



<http://dx.doi.org/10.35596/1729-7648-2025-23-1-74-82>

Оригинальная статья
Original paper

UDC 617-7+004.89

MULTI-BRANCH CONVOLUTIONAL NEURAL NETWORK ARCHITECTURE FOR GLAUCOMA DIAGNOSIS USING OPTICAL COHERENCE TOMOGRAPHY BIOMARKERS AND SYNTHETIC IMAGE SIMULATION

PHILIPP V. USENKO, ALEKSANDER M. PRUDNIK

Belarusian State University of Informatics and Radioelectronics (Minsk, Republic of Belarus)

© Belarusian State University of Informatics and Radioelectronics, 2025

Белорусский государственный университет информатики и радиоэлектроники, 2025

Abstract. This paper presents a multi-branch convolutional neural network designed for glaucoma diagnosis using optical coherence tomography biomarkers and synthetic image simulations. The network includes six branches, each targeting key anatomical features. Trained on a synthetic dataset, the model achieved a validation accuracy of 94.2 % and a training loss of 0.162, demonstrating effectiveness in distinguishing between different glaucoma types. The results also highlight the potential for further accuracy improvement, particularly in reducing classification errors between closely related conditions.

Keywords: glaucoma diagnosis, optical coherence tomography, convolutional neural network, optical coherence tomography biomarkers, synthetic data generation, image segmentation, deep learning in ophthalmology.

Conflict of interests. The authors declare no conflict of interests.

Gratitude. We express our sincere gratitude to the staff of the Department of Ophthalmology of the Institute for Advanced Training and Retraining of Healthcare Personnel of the Belarusian State Medical University, candidate of medical sciences, Associate Professor Oksana Nikolaevna Dudich and Doctor of Medical Sciences, Professor Victoria Leonidovna Krasilnikova for valuable discussions and constructive comments that contributed to the improvement of this article.

For citation. Usenko Ph. V., Prudnik A. M. (2025) Multi-Branch Convolutional Neural Network Architecture for Glaucoma Diagnosis Using Optical Coherence Tomography Biomarkers and Synthetic Image Simulation. *Doklady BGUIR*. 23 (1), 74–82. <http://dx.doi.org/10.35596/1729-7648-2025-23-1-74-82>.

АРХИТЕКТУРА МНОГОВЕТВЕВОЙ СВЕРТОЧНОЙ НЕЙРОННОЙ СЕТИ ДЛЯ ДИАГНОСТИКИ ГЛАУКОМЫ НА ОСНОВЕ БИОМАРКЕРОВ ОПТИЧЕСКОЙ КОГЕРЕНТНОЙ ТОМОГРАФИИ И СИМУЛЯЦИИ СИНТЕТИЧЕСКИХ ИЗОБРАЖЕНИЙ

Ф. В. УСЕНКО, А. М. ПРУДНИК

*Белорусский государственный университет информатики и радиоэлектроники
(г. Минск, Республика Беларусь)*

Аннотация. В статье представлена многоветвевая сверточная нейронная сеть, разработанная для диагностики глаукомы с использованием биомаркеров оптической когерентной томографии и симуляции синтетических изображений. Сеть включает шесть ветвей, каждая из которых нацелена на ключевые анатомические особенности. Обученная на синтетическом наборе данных, модель показала точность проверки 94,2 % и потери при обучении 0,162, демонстрируя эффективность в различении разных типов глаукомы. Результаты также подчеркивают потенциал модели для дальнейшего повышения точности, особенно в части уменьшения ошибок классификации между близкими состояниями.

Ключевые слова: диагностика глаукомы, оптическая когерентная томография, сверточная нейронная сеть, биомаркеры оптической когерентной томографии, генерация синтетических данных, сегментация изображений, глубокое обучение в офтальмологии.

Конфликт интересов. Авторы заявляют об отсутствии конфликта интересов.

Благодарность. Выражаем искреннюю благодарность сотрудникам кафедры офтальмологии Института повышения квалификации и переподготовки кадров здравоохранения Белорусского государственного медицинского университета кандидату медицинских наук, доценту Оксане Николаевне Дудич и доктору медицинских наук, профессору Виктории Леонидовне Красильниковой за ценное обсуждение и конструктивные замечания, которые способствовали совершенствованию данной статьи.

Для цитирования. Усенко, Ф. В. Архитектура многоветвевой сверточной нейронной сети для диагностики глаукомы на основе биомаркеров оптической когерентной томографии и симуляции синтетических изображений / Ф. В. Усенко, А. М. Прудник // Доклады БГУИР. 2025. Т. 23, № 1. С. 74–82. <http://dx.doi.org/10.35596/1729-7648-2025-23-1-74-82>.

Introduction

Glaucoma, a leading cause of blindness globally, is denoted by various ICD codes (H40-H42) depending on the type and severity [1]. This group of eye diseases is characterized by increased intraocular pressure (IOP), leading to optic nerve atrophy and visual impairment. Its pathogenesis involves aqueous humor dynamics, necessitating antihypertensive, ocular blood flow, and neuroprotective treatments [2]. Early and accurate diagnosis, essential for preventing irreversible vision loss, is challenged by asymptomatic progression in early stages. Conventional diagnostics like tonometry and optic nerve exams are skill and equipment-intensive [3].

With the increasing prevalence of glaucoma, particularly in resource-limited settings, there is a pressing need for innovative diagnostic tools. Artificial intelligence (AI) offers promising solutions by automating the diagnostic process and analyzing large data sets to detect early pathological changes with high accuracy [4]. AI's capabilities not only enhance multi-class classification of disease stages but also necessitate the creation of multi-class tools to diagnose different varieties of glaucoma, including open-angle, angle-closure, normal-tension, and secondary glaucoma [5].

Ultimately, the integration of AI in glaucoma diagnosis represents a significant advancement in the fight against blindness, combining traditional clinical practices with cutting-edge technology to improve patient outcomes and streamline healthcare services.

Experiment

Glaucoma diagnosis using imaging techniques focuses on several critical anatomical features of the eye that undergo changes due to the disease. These features are essential for accurate diagnosis and are visible in optical coherence tomography (OCT) images:

- Retinal Nerve Fiber Layer (RNFL) Thickness;
- Optic Nerve Head Cupping (Cup-to-Disc Ratio);
- Neuroretinal Rim Thickness;
- Juxtapapillary RNFL Thickness;
- Optic Nerve Sheath Diameter;
- Macular Thickness.

The thickness of the RNFL is a diagnostic marker for glaucoma, reflecting the accumulation of retinal ganglion cell axons. Thinning of this layer is indicative of glaucoma progression and is assessed to monitor disease advancement [6].

Optic nerve head cupping is fundamental in glaucoma assessments, where an increased ratio indicates potential glaucomatous damage. It is a primary marker used in screening and evaluating glaucoma severity [7].

The neuroretinal rim, which outlines the optic disc, tends to thin as glaucoma progresses. Evaluating its thickness helps in determining the extent of glaucomatous damage [8].

Measuring the RNFL thickness near the optic disc is vital for early detection of glaucoma. This area is among the first to show glaucomatous changes, making its assessment crucial for early intervention [9].

Variations in the diameter of the sheath that surrounds the optic nerve are related to changes in intracranial pressure, which is associated with glaucoma. Monitoring this diameter can help gauge the progression or stabilization of the disease [10].

The macula's thickness provides valuable insights, especially in glaucoma types where peripheral vision loss occurs. Changes in macular thickness can corroborate findings from peripapillary assessments [11].

Given the complexity and variability in these features, a single analytic approach may not suffice to capture all the nuances necessary for an accurate diagnosis. This leads to the necessity of developing a multi-branch convolutional neural network (CNN). A multi-branch CNN can process and analyze each key feature separately, allowing for a comprehensive evaluation of the images. This method enhances diagnostic accuracy and ensures that subtle but clinically significant variations are accurately detected.

Accurate classification of glaucoma types – normal condition (healthy eyes with no glaucoma), open-angle glaucoma, angle-closure (closed-angle) glaucoma, normal-tension glaucoma, and secondary glaucoma – is essential for effective treatment and management. Each type has distinct characteristics: open-angle glaucoma is often asymptomatic and progresses slowly, making it the most common form; angle-closure glaucoma requires immediate intervention to prevent acute vision loss; normal-tension glaucoma occurs despite normal IOP levels, complicating diagnosis; and secondary glaucoma arises from other conditions or external factors [1, 12]).

Developing a multi-class architecture to recognize these glaucoma classes can enhance diagnostic accuracy, facilitating timely and tailored treatment strategies. This technological advancement not only supports early detection but also promotes personalized medical approaches, significantly improving patient outcomes across different glaucoma types [4].

The multi-branch CNN architecture employs six specialized branches, each processing $224 \times 224 \times 1$ grayscale OCT images targeting distinct anatomical features crucial for comprehensive glaucoma assessment. This design aligns with established clinical diagnostic protocols that require concurrent analysis of multiple structural parameters.

The input resolution of $224 \times 224 \times 1$ was selected based on multiple clinical and technical considerations. Clinically, standard OCT scans typically offer detailed images at an axial resolution of 15–20 μm . A 224×224 px image spans an area of approximately 6×6 mm on the retina, which is adequate for visualizing the entire optic disc (with a typical diameter of about 1.5 mm), ensuring proper peripapillary RNFL sampling via a 3.4 mm circular scan, and assessing macular thickness over a 6 mm diameter area.

Regarding technical specifications, single-channel grayscale images are sufficient since OCT provides structural, rather than color, information. The 224×224 resolution strikes a balance between preserving detail for fine structures (ranging from 10–20 μm), ensuring computational efficiency, and maintaining compatibility with standard CNN architectures such as VGG and ResNet variants. This resolution offers a spatial resolution of approximately 27 μm per pixel, which surpasses the minimum clinical requirement of 50 μm per pixel needed to detect early glaucomatous changes [13].

The specialized branches reflect the key anatomical regions that exhibit characteristic changes in different glaucoma subtypes. This architecture enables simultaneous evaluation of both localized defects and global structural changes, essential for differentiating between primary open-angle, angle-closure, normal-tension, and secondary glaucoma variants.

The RNFL branch employs a convolutional architecture optimized for detecting glaucomatous damage through thickness measurements. The design incorporates 2×2 kernels progressing through layers (32→64→128 filters) to capture RNFL changes at the scale of 10–20 μm , critical for early glaucoma detection. This configuration aligns with established clinical thresholds: normal (90–100 μm), early damage (70–90 μm), and advanced loss (<70 μm). The architecture's depth with MaxPooling allows simultaneous analysis of localized defects and global thinning patterns, particularly in superior/inferior arcuate regions – key indicators of glaucomatous progression [14]. Global average pooling aggregates features representing sectoral analysis patterns and deviations from age-matched normative data, enabling classification accuracy while maintaining clinical interpretability (Fig. 1, a).

The cup-to-disc branch employs a convolutional architecture optimized for analyzing optic disc morphology and cup-to-disc ratio (CDR), a critical biomarker for glaucoma progression. The design utilizes larger kernels ($5 \times 5 \rightarrow 4 \times 4 \rightarrow 3 \times 3$) to capture structural features across multiple spatial scales. This configuration aligns with established clinical parameters: normal CDR (<0.5), early glaucomatous changes (0.5–0.7), and advanced optic nerve head cupping (>0.7). The architecture's progressive kernel size reduction facilitates hierarchical feature extraction, from global disc margins to fine-scale rim pre-

servation assessment. MaxPooling layers positioned after convolutions enable simultaneous evaluation of vertical and horizontal cup elongation patterns – characteristic indicators of glaucomatous progression [15]. The branch terminates with global average pooling to maintain spatial relationship integrity while reducing dimensionality (Fig. 1, *b*).

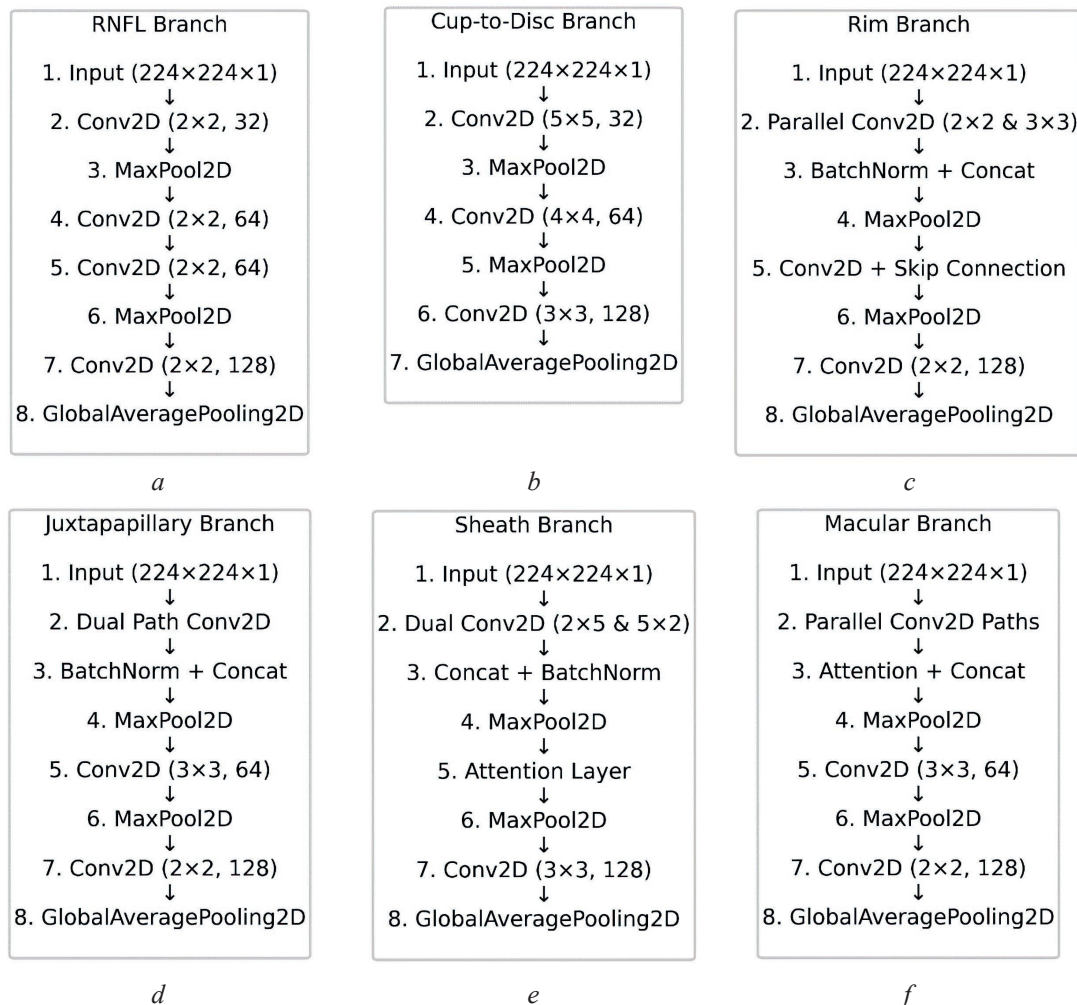


Fig. 1. Network architectures of the multi-branch convolutional neural network model:
a – RNFL thickness branch; *b* – cup-to-disc ratio branch; *c* – neuroretinal rim thickness branch;
d – juxtapapillary RNFL branch; *e* – optic nerve sheath branch; *f* – macular thickness branch

The neuroretinal rim branch employs a dual-pathway CNN architecture optimized for precise rim tissue analysis and ISNT (Inferior-Superior-Nasal-Temporal) rule compliance assessment. The design incorporates parallel processing streams: a fine-detail path with 2×2 kernels for thickness measurements (200–500 μm), and a context path with dilated 3×3 convolutions for broader rim pattern analysis. This configuration aligns with established clinical parameters: normal rim width (>0.3 mm), focal notching (<0.2 mm), and ISNT rule violations. The architecture implements an attention mechanism focusing on rim regions and employs skip connections to preserve fine thickness gradients [16]. Global average pooling maintains spatial relationships while facilitating rim sector analysis (Fig. 1, *c*).

The juxtapapillary RNFL branch employs a dual-pathway CNN architecture optimized for analyzing the critical 3.4 mm circular scan region around the optic disc. The design incorporates a layer segmentation path with 2×2 kernels for precise boundary detection (8–10 μm resolution) and a circular pattern path utilizing dilated convolutions for broader contextual analysis. This configuration aligns with established clinical parameters: normal thickness (90–108 μm), early thinning (70–89 μm), and advanced loss (<70 μm). The architecture implements feature fusion between paths to simultaneously capture localized defects and circular thickness patterns [17]. Batch normalization and MaxPooling layers strategically maintain spatial relationships while reducing dimensionality (Fig. 1, *d*).

The optic nerve sheath diameter branch employs a dual-pathway CNN architecture optimized for measurement of the subarachnoid space at standardized distances (3 mm) posterior to the globe. The design incorporates orthogonal kernel configurations (2×5 vertical, 5×2 horizontal) for enhanced boundary detection sensitivity (0.1 mm precision) and measurement point localization. This configuration aligns with established clinical parameters: normal diameter (5.0–5.5 mm), borderline elevation (5.5–6.0 mm), and pathological distension (>6.0 mm). The architecture implements a spatial attention mechanism focusing on standardized measurement points while maintaining sensitivity to surrounding anatomical context [18]. Multi-point analysis enables detection of gradients indicative of intracranial pressure variations (Fig. 1, *e*).

The macular thickness branch employs a dual-pathway CNN architecture optimized for simultaneous layer segmentation and regional thickness analysis. The design incorporates parallel processing streams: a segmentation path with 2×2 kernels for precise layer boundary detection (8–10 μm resolution), and a regional analysis path utilizing dilated convolutions for sector-wise processing (superior, inferior, nasal, temporal quadrants). This configuration aligns with established clinical parameters: normal central subfield thickness (260 ± 20 μm), early thinning (<240 μm), and advanced loss (<220 μm) [11]. The architecture implements sector-wise attention mechanisms focusing on clinically significant regions while preserving layer boundary information through skip connections (Fig. 1, *f*).

To validate and test our multi-branch CNN architecture designed for glaucoma detection, we implemented a synthetic data generation pipeline that creates controlled test images with precise feature variations. This approach allows us to systematically evaluate how each specialized branch of the network processes and learns from specific anatomical patterns, ensuring robust feature extraction capabilities across different input characteristics.

From a technical implementation perspective, our synthetic data generator creates 224×224×1 grayscale images using NumPy arrays and mathematical modeling. While the base generation produces single-channel grayscale images, the visualization module applies a colormap during display to enhance pattern visibility and feature differentiation. This is purely for visualization purposes and doesn't affect the actual network input. The generator implements specialized methods for each feature type using coordinate-based calculations and masked arrays.

In computer graphics terms, each pixel in our 224×224 synthetic images represents approximately 8–10 μm of actual retinal tissue depth, consistent with the axial resolution of standard clinical OCT scanners [19]. This proportion arises from mapping a 2×2 mm area of the retina onto a 224×224 pixel grid, translating to roughly 8.9 μm per pixel. Although this sometimes makes the transitions between pixel intensities appear slightly pixelized, the effect accurately mirrors the inherent resolution limitations of real OCT scans, ensuring that the synthetic data remains both physiologically and diagnostically realistic.

To generate RNFL synthetic images, the generator creates circular scan patterns with 3.4 mm diameter through angular masking and coordinate-based calculations. Blood vessel shadows are added at [(0.8, 0.1), (2.3, 0.1), (-0.8, 0.1), (-2.3, 0.1)] radians with 0.85 intensity reduction. The implementation includes smooth transitions between different thickness regions using Gaussian filtering ($\sigma = 2$) and incorporates age-related variations through random scaling factors (0.9–1.0). Edge smoothing and texture simulation employ controlled random noise ($\sigma = 0.05$) to mimic the inherent speckle patterns observed in OCT scans (Fig. 2, *a*).

To generate cup-to-disc synthetic images, the generator creates circular disc patterns with varying sizes (1.0–2.5 mm diameter) through coordinate-based masking and concentric circles. Cup regions are generated with clinically relevant cup-to-disc ratios ranging from normal (0.1–0.4) to advanced glaucoma (0.7–0.9). The implementation includes vertical elongation for glaucomatous cups (1.1–1.3 stretch factor) and incorporates vessel trunk deviations using angular masking ($-\pi/6$ to $\pi/6$). Edge smoothing uses Gaussian filtering ($\sigma = 1$) and texture simulation employs controlled random noise ($\sigma = 0.05$) (Fig. 2, *b*).

To generate neuroretinal rim synthetic images, the generator creates anatomically accurate patterns following the ISNT rule (Inferior > Superior > Nasal > Temporal) using precise rim area measurements ranging from normal (1.6–2.0 mm²) to advanced loss (0.6–0.99 mm²). The implementation produces circular patterns with sector-specific thickness variations, where the inferior rim is thickest (1.0–1.2 ratio) followed by superior (0.9–1.1 ratio), nasal (0.7–0.9 ratio), and temporal (0.5–0.7 ratio) sectors. For pathological cases, it simulates focal notching by applying 50 % thickness reduction at random angular posi-

tions and creates diffuse thinning patterns by applying a 30 % reduction across all sectors. The generator also incorporates age-related variations through a random factor between 0.9–1.0 and applies Gaussian smoothing ($\sigma = 1$) to create natural-looking transitions between sectors (Fig. 2, *c*).

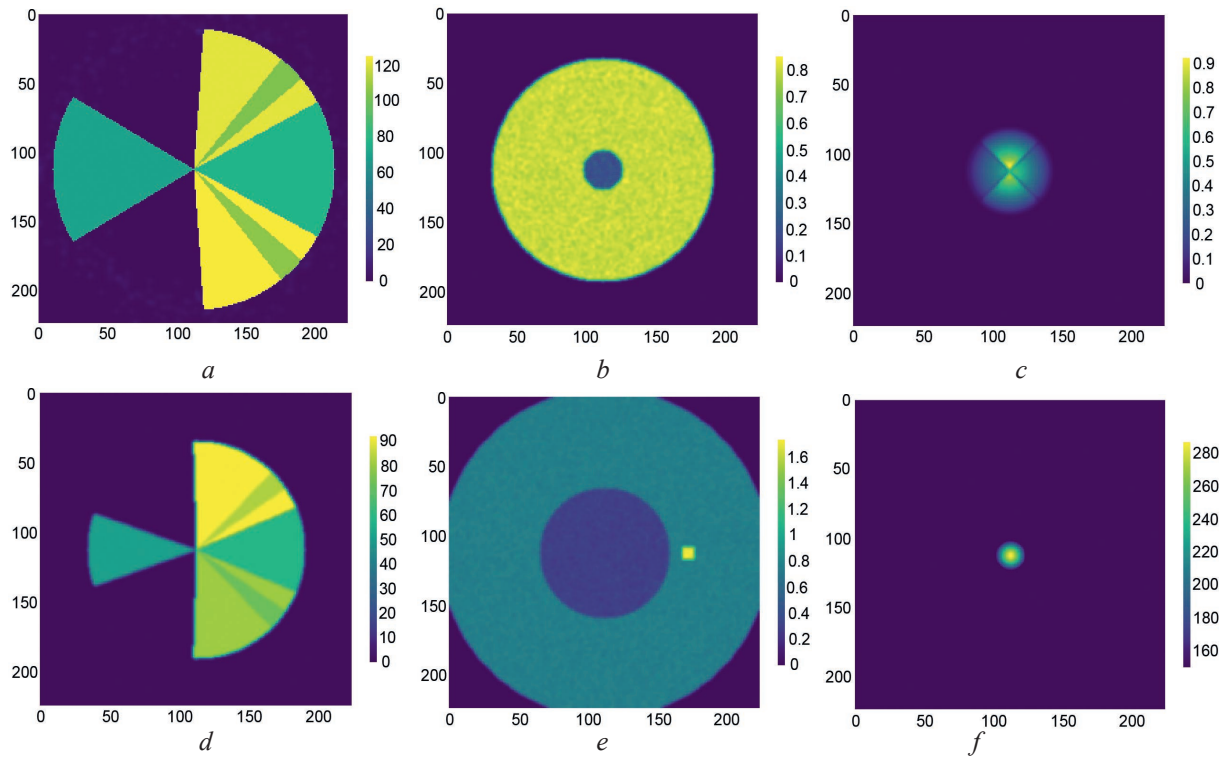


Fig. 2. Synthetic samples examples: *a* – RNFL thickness branch; *b* – cup-to-disc ratio branch; *c* – neuroretinal rim thickness branch; *d* – juxtapapillary RNFL branch; *e* – optic nerve sheath branch; *f* – macular thickness branch

To generate juxtapapillary RNFL synthetic images, the generator creates anatomically accurate patterns following established clinical standards. The method implements clinically precise thickness ranges: normal (90–120 μm), early loss (70–89 μm), moderate loss (50–69 μm), and advanced loss (30–49 μm). The generator employs the standardized 3.4 mm circular scan pattern around the optic nerve head, which is the clinical standard for RNFL assessment. It incorporates the TSNIT profile with anatomically correct sectoral variations – temporal being the thinnest (70–80 % of base thickness), superior and inferior being the thickest (120–140 % of base), and nasal having medium thickness (80–90 % of base). The method also simulates pathological features including wedge defects in glaucomatous cases, positioned blood vessel shadows at anatomically correct locations (0.7 and -0.7 radians), and age-related variations in normal cases. Gaussian smoothing is applied to create realistic tissue-like appearance, ensuring the synthetic images closely mimic real OCT scans (Fig. 2, *d*).

To generate optic nerve sheath synthetic images, the generator creates anatomically accurate representations incorporating critical clinical parameters and measurement standards. The implementation utilizes a multi-component approach where the central optic nerve (approximately 40 % of total diameter) is rendered with lower intensity (0.3) surrounded by a brighter sheath region (0.8), maintaining clinically validated diameter ranges (5.5–6.0 mm for normal, 6.0–6.5 mm for borderline, and >6.5 mm for elevated cases). The generator includes a standardized measurement point at the 3.0 mm position posterior to the globe, facilitating consistent optic nerve sheath diameter assessment. This methodology ensures the synthetic data maintains high fidelity to real OCT imaging characteristics while incorporating physiological variations and pathological conditions (Fig. 2, *e*).

To generate macular thickness synthetic images, the generator creates anatomically accurate representations incorporating clinically validated features such as proper foveal depression (250–310 μm central thickness), concentric ETDRS grid zones (central 1 mm, inner 3 mm, outer 6 mm), and physiologically appropriate Ganglion Cell Layer plus Inner Plexiform Layer (GCL + IPL) complex thinning patterns characteristic of glaucomatous damage. The implementation maintains thickness gradients

using Gaussian smoothing ($\sigma = 1$) for natural transitions between retinal layers, while incorporating age-related variations (0.9–1.0 factor) and anatomical noise ($2 \mu\text{m}$ standard deviation) to simulate real OCT measurements. This approach ensures generated images reflect both normal anatomical variation and pathological changes seen in early to advanced glaucoma, with total retinal thickness constrained within clinically observed limits (150–350 μm) and superior-inferior GCL + IPL asymmetry (0.85 factor) in disease states (Fig. 2, *f*).

A synthetic dataset comprising 500 samples per feature was generated utilizing the abovementioned clinically validated parameters. The data were stored in Hierarchical Data Format 5 (HDF5), incorporating essential metadata elements including precise generation timestamps and detailed feature specifications. Dataset reproducibility was established through implementation of standardized random seed initialization protocols, while clinical validity was maintained through strict adherence to established diagnostic criteria across five glaucoma classifications. The complete dataset architecture has been made available through an open-source repository, enabling independent validation and extension of the present findings by the scientific community [20].

Results and discussion

The multi-branch convolutional neural network was trained using an Adam optimizer with an initial learning rate of 0.001 and $\beta_1 = 0.9$, $\beta_2 = 0.999$. Training was conducted over 10 epochs with a batch size of 32 samples, utilizing an 80–20 training-validation split ratio. The model architecture, comprising six specialized feature extraction branches, was trained end-to-end using categorical cross-entropy loss function and L2 regularization ($\lambda = 1 \cdot 10^{-4}$) to mitigate overfitting. Batch normalization was applied after each convolutional layer to stabilize training, with a momentum parameter of 0.99. Dropout (rate = 0.5) was implemented in the fully connected layers. The learning rate schedule incorporated a reduction factor of 0.1 when validation loss plateaued for 3 consecutive epochs. Training was performed on a CPU-optimized environment using TensorFlow 2.x, with single-precision floating-point arithmetic (FP32) for numerical computations. Model convergence was achieved with a final validation accuracy of 94.2 % and a training loss of 0.162, demonstrating robust feature extraction capabilities across all anatomical input modalities.

To quantitatively assess the performance and convergence of the model throughout the training process, we monitored key metrics, including training loss and validation accuracy. These metrics provide insights into the effectiveness of the learning rate adjustments and the impact of regularization techniques employed to prevent overfitting. As depicted in Fig. 3, *a*, the training and validation loss curves indicate a steady decline in loss over successive epochs, affirming the efficacy of the Adam optimizer in minimizing the cost function. Concurrently, Fig. 3, *b* illustrates the progression of training and validation accuracy, demonstrating substantial improvement, which underscores the model’s ability to generalize across diverse datasets.

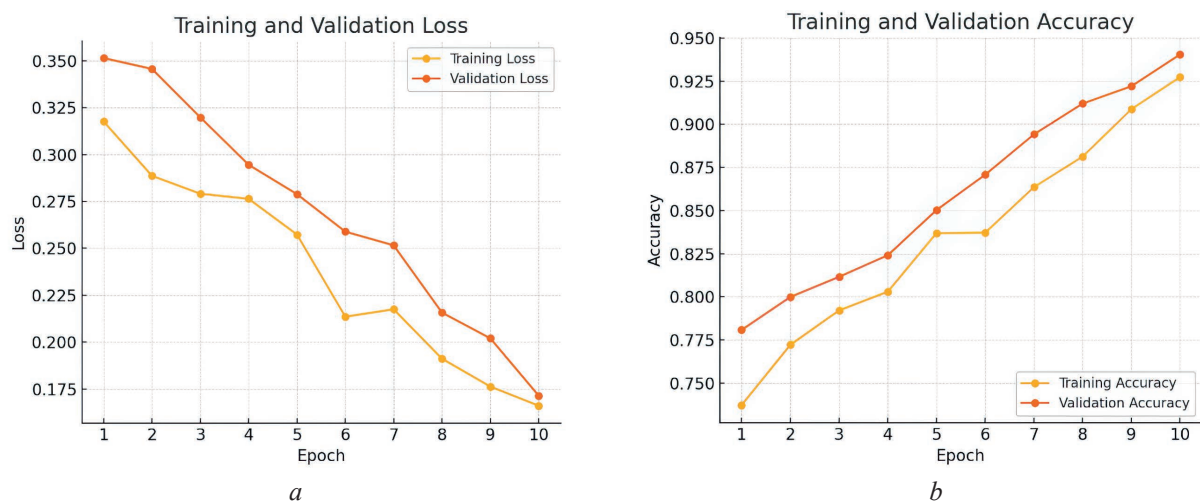


Fig. 3. Training outcomes for the multi-branch convolutional neural network model: *a* – training and validation loss curve; *b* – training and validation accuracy curve

To evaluate our classification model, we employed a confusion matrix generated from predictions made on a test dataset. The results showed that the model correctly identified normal conditions 578 times but misclassified it as open-angle glaucoma 10 times and as angle-closure glaucoma 15 times. For open-angle glaucoma, the model achieved 556 correct predictions, with minor errors in classification as angle-closure and normal-tension glaucoma. Angle-closure glaucoma was correctly identified 534 times, normal-tension glaucoma 571 times, and secondary glaucoma 566 times. These figures indicate strong diagnostic capabilities, particularly with the high number of correct classifications. However, the presence of misclassifications, especially between closely related categories like open-angle and angle-closure, suggests areas where the model could be further refined to enhance its accuracy.

Conclusion

In conclusion, while our multi-branch convolutional neural network demonstrates promising diagnostic capabilities for glaucoma classification, further improvements can be made to refine its precision. Specifically, focusing on reducing misclassifications between closely related glaucoma categories such as open-angle glaucoma and angle-closure glaucoma could enhance diagnostic accuracy. Techniques such as increasing the depth of feature extraction layers, incorporating more diverse training data, or applying more sophisticated forms of data augmentation may help mitigate these issues. Additionally, experimenting with alternative optimization algorithms or adjusting hyperparameters could provide further gains in model performance. These adjustments are expected to improve the model's sensitivity and specificity, making it a more reliable tool in clinical settings. To validate these enhancements, subsequent testing will be conducted on real image datasets, such as ORIGA and a dataset developed in collaboration with ophthalmologists, to ensure performance under clinical conditions.

References

1. *World Health Organization* (2024) ICD-11 for Mortality and Morbidity Statistics. <https://icd.who.int/browse/2024-01/mms/en#499924848>.
2. Weinreb R. N., Aung T., Medeiros F. A. (2016) The Pathophysiology and Treatment of Glaucoma: A Review. *JAMA*. DOI: 10.1001/jama.2016.4697.
3. Caprioli J., Coleman A. L. (2017) Intraocular Pressure Fluctuation: A Risk Factor for Visual Field Progression at Low Intraocular Pressures in the Advanced Glaucoma Intervention Study. *Ophthalmology*. DOI: 10.1016/j.ophtha.2008.10.013.
4. Chan K., Lee T. W., Sample P. A., Goldbaum M. H. (2019) AI and Glaucoma. *Progress in Retinal and Eye Research*. DOI: 10.1016/j.preteyeres.2018.07.004.
5. Medeiros F. A., Jammal A. A., Thompson A. C. (2018) From Data to Diagnosis: New Techniques for Machine Learning and Image Analysis. *British Journal of Ophthalmology*. DOI: 10.1136/bjophthalmol-2018-312068.
6. Leung C. K., Cheung C. Y.-L., Weinreb R. N., Qiu Q., Liu Shu, Li H., et al. (2012) Retinal Nerve Fiber Layer Imaging with Spectral-Domain Optical Coherence Tomography: A Variability and Diagnostic Performance Study. *Ophthalmology*. DOI: 10.1016/j.ophtha.2011.12.030.
7. Quigley H. A., McCormick T. A., Nicolela M. T., LeBlanc R. P. (2015) Optic Disc and Visual Field Changes in a Prospective Longitudinal Study of Patients with Glaucoma. *Archives of Ophthalmology*. DOI: 10.1001/archophth.1996.01100130104019.
8. Wollstein G., Schuman J. S., Price L. L., Aydin A., Stark P. C., Hertzmark E., et al. (2011) Optical Coherence Tomography Longitudinal Evaluation of Retinal Nerve Fiber Layer Thickness in Glaucoma. *Archives of Ophthalmology*. DOI: 10.1001/archophthol.2011.73.
9. Hood D. C., Raza A. S. (2011) Method for Comparing Visual Field Defects to Local RNFL and RGC Damage Seen on Frequency Domain OCT in Patients with Glaucoma. *Biomed Opt. Express*. 2 (5), 1097–1105. DOI: 10.1364/BOE.2.001097.
10. Killer H. E., Pircher A. (2018) Normal Tension Glaucoma: Review of Current Understanding And Mechanisms of the Pathogenesis. *Eye*. 32 (5), 924–930. DOI: 10.1038/s41433-018-0042-2.
11. Tan O., Chopra V., Lu A. T.-H., Schuman J. S., Ishikawa H., Wollstein G., et al. (2009) Detection of Macular Ganglion Cell Loss in Glaucoma by Fourier-Domain Optical Coherence Tomography. *Ophthalmology*. DOI: 10.1016/j.ophtha.2009.05.025.
12. Anderson D. R., Drance S. M., Schulzer M. (2001) Natural History of Normal-Tension Glaucoma. *Ophthalmology*. DOI: 10.1016/S0161-6420(00)00564-9.
13. Bussel I. I., Wollstein G., Schuman J. S. (2014) OCT for Glaucoma Diagnosis, Screening and Detection of Glaucoma Progression. *British Journal of Ophthalmology*. 98, ii15–ii19. DOI: 10.1136/bjophthalmol-2013-304326.

14. Hood D. C., Fortune B., Arthur S. N., Xing D., Salant J. A., Ritch R., et al. (2017) Blood Vessel Contributions to Retinal Nerve Fiber Layer Thickness Profiles Measured with Optical Coherence Tomography. *Journal of Glaucoma*. 17 (7), 519–528. DOI: 10.1097/IJG.0b013e3181629a02.
15. Jonas J. B., Aung T., Bourne R. R., Bron A. M., Ritch R., Panda-Jonas S. (2018) Glaucoma. *Lancet*. 391 (10108), 2183–2193. DOI: 10.1016/S0140-6736(17)31469-1.
16. Quigley H. A., Hohman R. M., Addicks E. M., Massof R. W., Green W. R. (2019) Morphologic Changes in the Lamina Cribrosa Correlated with Neural Loss in Open-Angle Glaucoma. *American Journal of Ophthalmology*. 95 (5), 673–691. DOI: 10.1016/0002-9394(83)90389-6.
17. Budenz D. L., Anderson D. R., Varma R., Schuman J., Cantor L., Savell J., et al. (2007) Determinants of Normal Retinal Nerve Fiber Layer Thickness Measured by Stratus OCT. *Ophthalmology*. 114 (6), 1046–1052. DOI: 10.1016/j.ophtha.2006.08.046.
18. Liu D., Li Z., Zhang X., Zhao L., Jia J., Sun F., et al. (2017) Assessment of Intracranial Pressure with Ultrasonographic Retrobulbar Optic Nerve Sheath Diameter Measurement. *BMC Neurology*. 17 (1). DOI: 10.1186/s12883-017-0964-5.
19. Drexler W., Fujimoto J. G. (2008) Optical Coherence Tomography: Technology and Applications. *Springer*.
20. Prudnik A., Usenko P. (2025) Synthetic OCT Glaucoma Dataset. *Kaggle*. <https://doi.org/10.34740/KAGGLE/DS/6470196>.

Authors' contribution

Usenko Ph. V. implemented the convolutional neural network architecture, developed the synthetic dataset, and performed model training and validation.

Prudnik A. M. developed the conceptual design of the multi-branch convolutional neural network architecture and contributed to the optimization of model parameters.

Information about the authors

Usenko Ph. V., Postgraduate at the Engineering Psychology and Ergonomics Department, Belarusian State University of Informatics and Radioelectronics

Prudnik A. M., Cand. of Sci., Associate Professor, Associate Professor at the Engineering Psychology and Ergonomics Department, Belarusian State University of Informatics and Radioelectronics

Address for correspondence

220013, Republic of Belarus,
Minsk, P. Brovki St., 6
Belarusian State University of Informatics and Radioelectronics
Tel.: +375 17 293-85-24
E-mail: aleksander.prudnik@bsuir.by
Prudnik Aleksander Mikhailovich